

Defect-induced magnetic structure of CuMnSb

F. Máca, J. Kudrnovský, and V. Drchal

Institute of Physics ASCR, Na Slovance 2, CZ-182 21 Praha 8, Czech Republic

I. Turek and O. Stelmakhovich

Charles University, Faculty of Mathematics and Physics,

Department of Condensed Matter Physics, Ke Karlovu 5, CZ-121 16 Prague 2, Czech Republic

P. Beran

Nuclear Physics Institute ASCR, CZ-250 68 Řež, Czech Republic

A. Llobet

Neutron Science and Technology, Physics, Los Alamos National Laboratory, Los Alamos, NM 87544, USA

X. Marti

Institute of Physics ASCR, Cukrovarnická 10, CZ-162 53 Praha 6, Czech Republic

(Dated: June 15, 2016)

Ab initio total energy calculations show that the antiferromagnetic (111) order is not the ground state for the ideal CuMnSb Heusler alloy in contrast to the results of neutron diffraction experiments. It is known, that Heusler alloys usually contain various defects depending on the sample preparation. We have therefore investigated magnetic phases of CuMnSb assuming the most common defects which exist in real experimental conditions. The full-potential supercell approach and a Heisenberg model approach using the coherent potential approximation are adopted. The results of the total energy supercell calculations indicate that defects that bring Mn atoms close together promote the antiferromagnetic (111) structure already for a low critical defect concentrations ($\approx 3\%$). A detailed study of exchange interactions between Mn-moments further supports the above stabilization mechanism. Finally, the stability of the antiferromagnetic (111) order is enhanced by inclusion of electron correlations in narrow Mn-bands. The present refinement structure analysis of neutron scattering experiment supports theoretical conclusions.

PACS numbers: 75.25.+z, 75.30.Et, 75.47.Np, 75.50.Ee

I. INTRODUCTION

Ferromagnetic Heusler and semi-Heusler alloys are materials with interesting physical properties. We refer the reader to a comprehensive recent review.¹ Several of them, due to their halfmetallic character, structural similarity with semiconductors, Curie temperatures above the room temperature, full spin polarization at the Fermi energy, and low magnetization damping are materials with potential in technological applications. The typical examples of such halfmetallic alloys are the semi-Heusler NiMnSb alloys, the full Heusler alloy Co₂FeGa or Mn₂CoAl with the inverse Heusler structure.

Halfmetallic Heusler alloys are usually ferromagnets, but there are also antiferromagnetic (AFM) alloys which can be potential materials for the so-called antiferromagnetic spintronics.² Recently the anisotropic magnetoresistance of the AFM-FeRh alloy was studied both experimentally and theoretically.³ The antiferromagnetism of CuMnSb Heusler alloys is well established,⁴ but its low critical Néel temperature limits practical applications as contrasted with the above-mentioned AFM FeRh alloys. A new family of CuMnX alloys, where X are elements of the fifth group with potentially higher critical temperature, was proposed recently and studied theoretically.

A promising candidate seems to be the layered CuMnAs alloy with a predicted Néel temperature in the range of room temperatures.^{5,6}

The halfmetallic CuMnSb, the first AFM Mn-based member of Heusler and semi-Heusler alloy family, therefore attracted the theoretical interest in the past, in particular as concerns its magnetic structure. A pilot first-principles study of its magnetic properties was the subject of Ref.7. Authors of this paper have compared the total energies of the non-magnetic, ferromagnetic (FM), and the AFM phases of CuMnSb at the experimental volume. They found, in agreement with the experiment, that the ground state is the AFM one. The total energy of the FM phase is higher while the total energy of the non-magnetic phase was found to be significantly above energies of the AFM and FM phases. The AFM phase was specifically chosen to be the AFM111 one, with the alternating (111)-planes of Mn atoms with aligned spins, as known from experimental neutron scattering studies.⁴

The fact that the theoretical situation can be more complex was indicated earlier in the study of (Cu,Ni)MnSb random alloys.⁸ The emphasis there was put on the explanation of unusual concentration dependence of magnetic moments and residual resistivities, namely, the dramatic change of the slope of the above

concentration dependencies for the Cu-content of 70-75%. However, different ab initio calculations found that the total energy of the ideal CuMnSb AFM100 structure is lower than the AFM111 phase detected experimentally. This result, obtained by the tight-binding linear muffin-tin orbital (TB-LMTO) method⁸ was also confirmed by our full-potential calculations.

Defects are very common in Heusler alloys and their type and amount depend strongly on the sample preparation and annealing procedure. Defects either preserve (swaps) stoichiometric composition or violate it (impurities). In the case of CuMnSb alloys, real experimental samples for which the magnetic structure was studied show relatively large residual resistivities of order $50 \mu\Omega\text{cm}$ (see, e.g., reference in Ref.7), which clearly indicates the presence of a non-negligible sample disorder. It is thus interesting to investigate how the presence of impurities will influence the magnetic stability of CuMnSb. A systematic study of formation energies of possible stoichiometric (swaps) and non-stoichiometric (antisite) defects in a closely related NiMnSb alloy was the subject of Ref.9. We will adapt this approach to the case of CuMnSb to identify the most probable defects according to their formation energies. A systematic estimate of formation energies of all possible defects is, however, beyond the scope of this paper. We limit ourselves to the most probable ones discussed in experiments¹⁰ or to those chosen by the analogy with the NiMnSb case⁹ and perform calculations in the framework of the TB-LMTO approach combined with the coherent potential approximation (CPA). The most probable defects seem to be Mn atoms on the Cu-sublattice, Mn_{Cu} , Cu atoms on the Mn-sublattice, Cu_{Mn} , Mn atoms at interstitial sites in the non-stoichiometric case, and the $\text{Cu} \leftrightarrow \text{Mn}$ swaps for the stoichiometric CuMnSb.

We study the effect of disorder on the magnetic structure due to the defects by two independent approaches: (i) the supercell approach employing the full-potential Vienna ab-initio simulation package (VASP),¹¹ and (ii) the Heisenberg model whose parameters were determined by the TB-LMTO-CPA approach¹² in which the effect of randomness is included in the framework of CPA. A main problem with supercell approach is the necessity to consider all probable AFM phases in the search for the ground state and also the large number of possible configurations which should be considered to simulate defect concentration dependencies. The Heisenberg model which describes directly the relevant magnetic part of total energy and does not assume any specific magnetic order as it starts from a completely random moment arrangement, can roughly indicate possible candidates. In this way we have extended the search also to the AFM40 phase (the A_2B_2 -type).¹³ The final search is then done using the supercell VASP approach due to its accuracy.

Another reason for the parallel study using the supercell and Heisenberg model is the fact that both methods represent limiting models of disordered systems. While the CPA provides a good description of completely dis-

ordered alloys neglecting the local environment or short-range order effects. The supercell approach, on the contrary, neglects the randomness of defects. While both approaches should agree reasonably well in the case of defects of one type (Mn_{Cu} -antisites or Mn-interstitials), in the case of two defects ($\text{Cu} \leftrightarrow \text{Mn}$ swaps) both models are very different. There is no correlation between positions of Mn_{Cu} - and Cu_{Mn} -antisites in the CPA while in the supercell approach we assume their fully correlated positions in the whole crystal (practically the nearest-neighbor positions to have computationally feasible sizes of supercells). Clearly, one thus can expect largest differences between both models for this case. The supercell approach also allows to check the robustness of results with respect to possible lattice relaxations which are neglected in the CPA. The real alloy is thus somewhere between these two limits.

The important characteristics of any magnetic system are magnetic, or exchange interactions among magnetic moments which enter the definition of the Heisenberg model. In the present case, these interactions are predominantly among Mn-moments. They are constructed using the first-principles Lichtenstein mapping procedure¹⁴ adapted to the TB-LMTO-CPA approach.¹⁵ It should be noted that this procedure allows to estimate directly interactions among moments at any pair of sites, and, in particular, also as a function of varying defect concentrations. This is very difficult in the supercell case. It is important to note that in the present case the exchange integrals are determined from the reference disordered local moment (DLM)¹⁶ state which describes material above the critical temperature (the paramagnetic state): no specific magnetic configuration is thus used in their construction, as emphasized above.

The most important result of the present study is the finding that already a low concentration of magnetic defects is able to change the system total energy in favor of the AFM111 phase so that defects can stabilize the AFM111 ground state of CuMnSb. Finally, we have also found that a proper treatment of electron correlations in narrow Mn d -bands⁷ is important and also helps to stabilize the AFM111 phase.

II. FORMALISM

The ideal CuMnSb has a C_{1b} crystal structure which can be represented by four fcc-type sublattices Cu-Mn-ES-Sb shifted along the [111]-direction of the parent fcc-lattice consecutively by the distance $\sqrt{3}/4a$, where a is the lattice constant and the symbol ES denotes the empty sublattice (interstitial sites). The AFM111/AFM100 magnetic structures consist of alternating [111]/[100] planes of Mn atoms with opposite spins which have doubled unit size as compared to the original C_{1b} lattice. Finally, the AFM40 magnetic structure is a tetragonal structure with alternating double layers of opposite spins along the [210]-direction (A_2B_2 -lattice).¹³ In

our calculations we use the experimental lattice constant $a = 6.088 \text{ \AA}^4$ and neglect small volume changes due to defects.

Two different electronic structure methods were used to determine the total energy of CuMnSb, both ideal and with specific defects, namely, the supercell VASP and TB-LMTO-CPA methods. Their technical details are summarized below.

The supercell VASP calculations were performed using the projector augmented wave scheme¹⁷ with different exchange correlation potentials. Only one defect in the unit cell is used for an antisite Mn or Cu atom or for Mn in interstitial position, while two nearest neighbor Mn and Cu-antisite defects are used to describe the Cu \leftrightarrow Mn swap. The magnetic supercell containing 12 atoms simulates an ideal crystal while supercells containing 24, 48, 96 and for some defects also 192 atoms simulate disordered alloys with defect concentrations of 12.5%, 6.25%, 3.13% and 1.56%, respectively. It should be noted that the presence of defects leads to a small finite total magnetic moment as contrasted with the exactly zero magnetic moment in the CPA method.

The Brillouin zone was sampled by $12 \times 12 \times 6$ k-points for the tetragonal unit cell with 24 atoms, and grids with correspondingly smaller number of sampling points were used for larger supercells. Identical large unit cell was used for AFM100, AFM111 and AFM40 magnetic structures for every defect concentration. The total energy error was 0.05 meV (per supercell), the difference between input and output charge densities in the final iteration of selfconsistent iterations was better than 0.1 me bohr^{-3} . For selected configurations we also optimized the local geometry by atomic force minimization. We found that local distortions have only weak effect on the total energy differences for small defect concentrations, therefore the most presented results are shown for unrelaxed structures. No lattice constant changes due to defects are considered.

In the TB-LMTO-CPA approach the effects of substitutional as well as magnetic disorders are described by the CPA neglecting possible lattice relaxations, local environment and clustering (short range order) effects.¹² In the disordered case we have used a simple screened impurity model¹⁸ to improve the treatment of alloy electrostatics. The *spdf*-basis and Vosko-Wilk-Nusair exchange correlation potential¹⁹ were used while integration over the full Brillouin zone was done using about 2000 k-vectors. The same Wigner-Seitz radii were used for all constituent atoms including the empty spheres that fulfill interstitial sites. Calculated total energies in the DLM state were used to estimate the formation energies of possible defects, swaps for the stoichiometric CuMnSb and impurities for the non-stoichiometric one. The selfconsistent DLM potentials were also used to estimate exchange interactions and to construct the Heisenberg Hamiltonian.

In both approaches we have optionally included the effect of electron correlations in narrow Mn-subbands

in the framework of the LDA+U method.²⁰ We employ the fully localized limit and make replacement $U_{\text{eff}} = U - J$, where U and J are, respectively, Coulomb repulsion and exchange constants. We used $U_{\text{eff}} = 0.13 \text{ Ry}$ which is similar to the value obtained in Ref.21 for a closely related NiMnSb Heusler alloy using the constrained random-phase approximation. The magnetic part of total energy is estimated from the classical Heisenberg Hamiltonian^{14,15}

$$H = - \sum_{i,j} J_{ij} \mathbf{e}_i \cdot \mathbf{e}_j, \quad (1)$$

where i, j are site indices, \mathbf{e}_i is the unit vector pointing along the direction of the local magnetic moment at site i , and J_{ij} is the exchange integral between sites i and j . The exchange integrals, by construction, contain the atom magnetic moments, their positive (negative) values being indicative of ferromagnetic (antiferromagnetic) coupling. It should be noted that for an evaluation of the exchange integrals we assume the DLM reference state in which possible small local moments on Cu, Sb, or interstitial sites vanish. The only non-zero exchange integrals are thus among Mn atoms. The DLM state assumes no prescribed magnetic order in the alloy, just the existence of local magnetic moments on Mn-atoms and conclusions drawn from it are thus very general. The DLM state can be naturally implemented in the framework of the TB-LMTO-CPA.¹⁶

In the case of random alloys the exchange interactions are usually approximated by the expression

$$J_{ij} = \sum_{QQ'} J_{ij}^{QQ'} \eta_i^Q \eta_j^{Q'} \quad (2)$$

in which η_i^Q are occupation indices ($\eta_i^Q = 1$ if site i is occupied by the atom of type Q and $\eta_i^Q = 0$ otherwise).

In the general case one should consider the dependence of vectors \mathbf{e}_i on the type of atom at the site i . The situation is simpler in the present case, because on each sublattice there is at most one type of magnetic atom. Consequently, the configurationally averaged energy is given by

$$\langle H \rangle = - \sum_{i,j} \sum_{QQ'} J_{ij}^{QQ'} \langle \eta_i^Q \eta_j^{Q'} \rangle \mathbf{e}_i \cdot \mathbf{e}_j. \quad (3)$$

Note that $J_{ij}^{QQ'} = 0$ for $i = j$ and the occupation indices belonging to different sites i and j average independently, $\langle \eta_i^Q \eta_j^{Q'} \rangle = x_i^Q x_j^{Q'}$, where x_i^Q are (local) concentrations. The averaged total energy ε per elementary cell, e.g., that corresponding to the specific magnetic phase, is then given by

$$\varepsilon = - \sum_i^{\text{cell}} \sum_j \tilde{J}_{ij} \mathbf{e}_i \cdot \mathbf{e}_j, \quad (4)$$

where

$$\tilde{J}_{ij} = \sum_{QQ'} J_{ij}^{QQ'} x_i^Q x_j^{Q'} \quad (5)$$

are effective exchange interactions. Calculated energies can be compared with those obtained from the corresponding total energy calculations based on the supercell VASP approach.

In the present approach we assume that magnetic moments have fixed size but allow their different spin directions when searching for the magnetic ground state. It should be noted that there exists a more general approach, the magnetic cluster expansion method,²² in which also the size of moments is a variational parameter. On the other hand, for an alloy with very rigid magnetic moments like, e.g., CuMnSb with Mn-moments, the present simpler approach is reasonable unless higher-order magnetic interactions become important.

III. RESULTS AND DISCUSSION

A. Magnetic ground state: the ideal CuMnSb

We shall start our discussion by investigating possible magnetic phases based on the Heisenberg model. The easiest way of doing so is to calculate the lattice Fourier transform $J(q)$ of exchange integrals (2) which enter the definition of the corresponding Heisenberg Hamiltonian (1). The $J(q)$ describes formally possible spin spirals on a given lattice. We shall employ two models: (i) in the first one leading interactions are obtained from the DLM phase which assumes no magnetic order, and (ii) two effective interactions are estimated from total energies of the FM, AFM100, and AFM111 phases calculated in the VASP. These interactions represent a fit of the three above energies onto the Heisenberg model and in some sense they include all interactions as determined above by first-principles mapping from the DLM phase. In both cases we used the LDA+U approach. The values are: $J_1/J_2 = -0.30/+0.013$ mRy for the DLM case, and $J_1/J_2 = -0.27/-0.034$ mRy for the VASP.

The result is shown in Fig. 1 in which, due to the minus sign in (1), the higher values correspond to lower energies and vice versa. Energies of such spin spirals correspond to specific magnetic phases, e.g., the values at $q = \Gamma, X, L$, and W relate to the FM, AFM100, AFM111, and AFM40 phases, respectively. A general magnetic phase diagram of Heusler alloys in the J_1/J_2 -plane was determined in Ref.23. In agreement with its predictions, we have the AFM100 ground state for the DLM case, but the AFM40 ground state for the VASP, although the AFM100 phase has almost identical energy. Both models thus predict that the AFM111 phase is not a ground state for the ideal CuMnSb. They also suggest that the AFM111, AFM100, and AFM40 are good candidates for the ground state (the FM phase can be excluded). The use of increased number of exchange integrals (62 shells) in the evaluation of $J(q)$ in the DLM case has only small effect. Calculations also predict that even more complex spin states could exist.

Using the above predictions, we present in Table I the

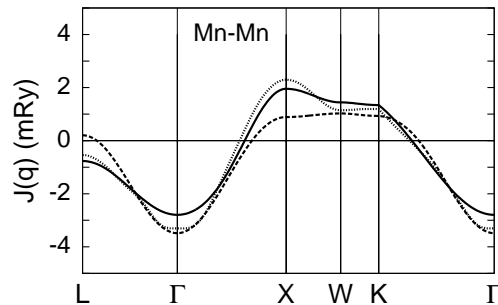


FIG. 1: Lattice Fourier transform $J(q)$ of the first two exchange interactions $J_{ij}^{\text{Mn,Mn}}$ for the ideal CuMnSb, obtained for the reference DLM state (full line) and derived from total energies for the FM, AFM100, and AFM111 phases in the VASP (dashed line). The case of 62 exchange interactions for the DLM state is shown in dots.

TABLE I: Total energy in meV per Mn atom for different phases of ideal CuMnSb and different type of electron exchange and correlation. The ordered structure AFM111 has been taken as reference $E_{\text{tot}}=0$.

	LDA ²⁴	GGA ²⁵	LDA+U ²⁰
AFM100	-0.89	-0.86	-0.52
AFM40	-1.14	-1.03	-0.55

total energies of such phases calculated using the VASP method. While all values shown correspond to the experimental lattice constant, we have also calculated total energies corresponding to the volume minimization for each phase and found only small differences which do not change the result. The VASP calculations agree well with predictions of the Heisenberg model. We mention in particular a correct relation of the AFM40 and AFM100 phases despite the fact that the former phase was not included in the estimate of J_1 and J_2 interactions.

B. Formation energies of defects

In this section we estimate formation energies of the most probable defects in CuMnSb, both in the stoichiometric (swapping defects) and non-stoichiometric (anti-site impurities) alloys. We employ the approach of Ref.9 used for a related NiMnSb Heusler alloy. The NiMnSb semi-Heusler alloys have high Curie temperatures around 750 K and the use of the reference FM state is well justified. On the other hand, CuMnSb has a very low (Néel) critical temperature of about 55 K, and in this case a reasonable reference state is the paramagnetic DLM state.

We will consider the following defects: (i) Mn-antisites on Cu, Mn-interstitials, i.e., Mn-rich CuMnSb sample, (ii) Cu-antisites on Mn, i.e., Cu-rich CuMnSb sample, and (iii) the following five swaps, namely, $\text{Cu} \leftrightarrow \text{Mn}$, $\text{Cu} \leftrightarrow \text{Vacancy}$, $\text{Cu} \leftrightarrow \text{Sb}$, $\text{Mn} \leftrightarrow \text{Vacancy}$, and $\text{Mn} \leftrightarrow \text{Sb}$.

These defects are considered as dominant ones both in the experiment¹⁰ and in the related theoretical study of NiMnSb⁹ (if one interchanges Ni and Cu). We determine the swap (sw) and defect (def) formation energies (FE) per formula unit using expressions

$$FE^{sw} = (E_{tot}^{sw} - E_{tot}^{id})/x_{sw} \quad (6)$$

and

$$FE^{def} = (E_{tot}^{def} - E_{tot}^{id} - x_{Cu}\mu_{Cu} - x_{Mn}\mu_{Mn} - x_{Sb}\mu_{Sb})/x_{def}, \quad (7)$$

respectively. Here, x_{sw} is the swap concentration, x_{def} is the concentration of the defect of the type D, μ_D is the chemical potential of the corresponding reservoir (D=Cu, Mn, or Sb), and corresponding total energies of ideal CuMnSb, CuMnSb with swaps, and CuMnSb with defects are denoted as E_{tot}^{id} , E_{tot}^{sw} , and E_{tot}^{def} , respectively. It should be noted that contrary to FE^{sw} , FE^{def} depend on the choice of chemical potentials. We calculate the chemical potentials as the energy per atom of the reservoir phase, i.e., the fcc-Cu, fcc-DLM Mn (LDA+U), and Sb in the diamond structure.

TABLE II: Formation energies (6) and (7) of selected defects (eV per formula unit) in the DLM-CuMnSb estimated using the TB-LMTO-CPA-LDA+U approach. ES stands for the vacancy. Calculations were done for the defect concentration $x = 0.05$ in each case.

Mn _{Cu}	Cu _{Mn}	Mn _{ES}	Cu↔Mn
0.292	0.666	0.730	1.016
Cu↔ES	Mn↔ES	Mn↔Sb	Cu↔Sb
2.482	3.231	3.280	7.446

In Table II we show formation energies of three typical defects for Mn- and Cu-rich CuMnSb alloys. The most energetically favorable defect is the Mn-antisite on the Cu sublattice, the Cu-antisite on the Mn sublattice and the Mn interstitial defect. The estimated formation energies for some of possible swaps are also shown. The lowest formation energy corresponds to the Cu↔Mn swap similarly as in the related NiMnSb alloy for Ni↔Mn swap.⁹ It should be noted that present calculations neglect the local environment effects which, as demonstrated for NiMnSb, generally lower formation energies as compared to those obtained using the CPA.⁹

C. Magnetic ground state: CuMnSb with defects

Non-stoichiometry and intermixing of Cu and Mn can be present in real materials. Mn atoms become the bonding neighbors of regular Mn atoms with much stronger exchange coupling that may overbalance the exchange energy due to interactions within the Mn sublattice, and reverse the order of total energies for AF100 and AF111. The defects which are present in real samples can stabilize the AFM111 phase. We consider only defects that

may appear with the highest probability, i.e., those with the lowest formation energies. To this end we employ total energies calculated as functions of the impurity concentrations for various magnetic states. The main results were obtained in the framework of the supercell VASP approach, but we also present results obtained using the Heisenberg Hamiltonian based on the paramagnetic (DLM) state. As explained above, the main reason for this is to illustrate the effect of different treatments of disorder, namely, the supercell approach and the CPA, on the magnetic stability. We consider the following defects: (i) Mn antisites on Cu sublattice, (ii) Mn interstitials, (iii) Cu antisites on Mn sublattice, and (iv) Mn↔Cu swaps. In the case (iv) the chemical composition is unchanged, while in the former cases the system is off-stoichiometric, either Mn-rich (cases (i) and (ii)), or Cu-rich (case (iii)) ones.

TABLE III: Ground states of various defects for $x > x_c$, x_c is a critical crossover concentration of defects. The impurity is Mn↑ or Cu. Mn impurity has additionally 4 Sb nearest-neighbors (NN), which is not shown. Index ap denotes the AFM phase with antiparallel alignment of defect Mn-moments to the moments on the native Mn-sublattice.

defect	ground state	NN atoms of Mn↑
Cu↔Mn NN swap	AFM40	1 Cu 1 Mn↑ 2 Mn ↓
Cu↔Mn swap	AFM111 _{ap}	1 Mn↑ 3 Mn↓
Mn _{Cu}	AFM111 _{ap}	1 Mn↑ 3 Mn↓
Mn interstitial	AFM111 _{ap}	1 Mn↑ 3 Mn↓
Cu _{Mn}	AFM40	4 Cu

The results of the supercell calculations for various defect types and varying concentrations are summarized in Fig. 2 and Table III. The following conclusions can be made: (i) The most favorable defect stabilizing AFM111 phase is the Mn-antisite on Cu lattice (Fig. 2a,b). For this case we have also shown the effect of lattice relaxations. The Mn ↑ substituting Cu prefers the Mn nearest neighbors with magnetic moments ↑↓↓↓, its magnetic moment (lower than magnetic moments of atoms on the Mn-sublattice) is oriented in our naming convention *antiparallel* (see Table III). The critical concentration for which the AFM111 is stabilized is less than 3% and the effect of lattice relaxations is negligible. We thus neglect their effect also for other defect types. (ii) Mn interstitials also stabilize the AFM111 phase although their effect is not so strong, the AFM111 phase is stabilized above about 6% (Fig. 2c). (iii) Cu antisites on Mn lattice are unable to stabilize the AFM111 phase at low defect concentrations observed in experiment, although they also slightly promote it (Fig. 2d); (iv) For the case of Mn-antisites on Cu lattice we demonstrate the effect of electron correlations by comparing the LDA, GGA, and LDA+U results for AFM40 to AFM111 crossover (see Fig. 3). The critical concentration is reduced about two times by correlation effects in comparison with the LDA and slightly less in comparison with the GGA case. It should be noted that

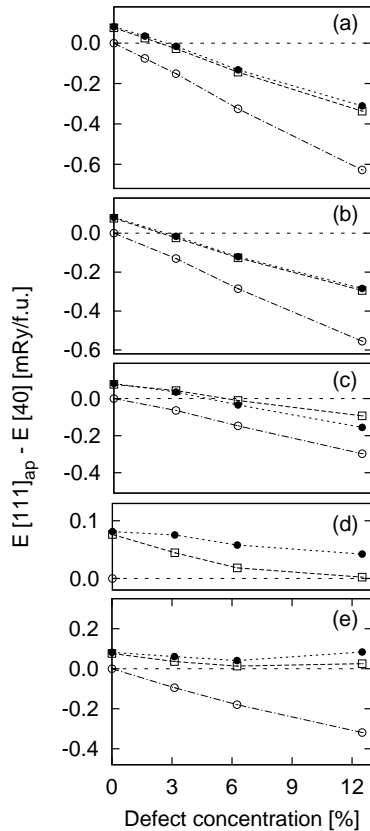


FIG. 2: The total energy differences $E[111]_{\text{ap}} - E[X]$ between the reference AFM111_{ap} state and corresponding antiferromagnetic configuration X as a function of concentrations of the following defects: (a) Mn antisites on Cu; (b) Mn antisites on Cu but with relaxed geometry; (c) Mn interstitials; (d) Cu antisites on Mn; and (e) Cu ↔ Mn swaps as obtained from VASP calculations. Index ap denotes the AFM phase with antiparallel alignment of defect Mn-moments to the moments on the native Mn-sublattice.

low concentrations of defects which stabilize the AFM111 phase are on the border of the accuracy of experimental methods currently used for structural studies, namely, the X-ray spectroscopy and the neutron scattering experiment (see Sec. III E for more details concerning the experiment).

Results based on the Heisenberg Hamiltonian are shown in Fig. 4. We emphasize that these results were obtained from the DLM reference state assuming no magnetic preference and neglecting the local environment effects. We see a good agreement with the supercell results in particular for the AFM40 phase for Mn-antisite on Cu, Mn-interstitial, and Cu-antisite on Mn, although the calculated critical concentrations are larger.

A possible relevance of local environment effects on the magnetic stability can be illustrated on Cu ↔ Mn swaps

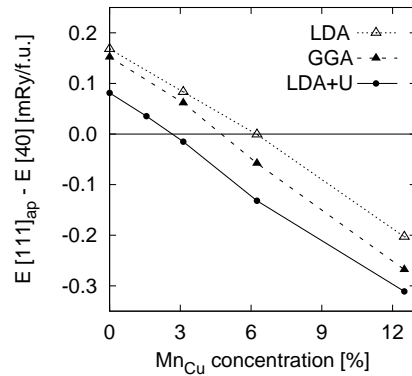


FIG. 3: The total energy differences of antiferromagnetic configurations $E[111]_{\text{ap}} - E[40]$ calculated with different exchange and correlation potentials as functions of Mn_{Cu} concentrations. The results for LDA,²⁴ GGA,²⁵ and LDA+U²⁰ are presented for unrelaxed structures. Index ap denotes the AFM phase with antiparallel alignment of defect Mn-moments to the moments on the native Mn-sublattice.

(see Fig. 2e and Fig. 4d for the supercell and Heisenberg models, respectively). While the Heisenberg model predicts the stabilization of the AFM111 phase by swaps the supercell approach does not. The explanation consists in very different ways of modeling of swaps in both approaches: while in the supercell approach we assume nearest-neighbor (NN) Cu ↔ Mn swap in the whole crystal, in the Heisenberg model based on the CPA we have completely uncorrelated Cu and Mn antisites. This result thus shows the dependence of present predictions based on small unit cell calculations on the local environment effects, in particular for swaps (see Table III). The CPA model is more realistic in this case. We can summarize that the stabilization of the AFM111 phase by small concentrations of defects with the lowest formation energies is an acceptable assumption to explain existing experimental data confirming the AFM111 state for CuMnSb alloy. Our model calculations show that the exchange coupling between the NN pairs of Mn atoms on two different sublattices stabilizes the AFM111 order. We will therefore analyze exchange interactions in more detail in the next Section.

D. Exchange interactions

Exchange integrals between Mn-moments in both ideal CuMnSb and CuMnSb with Mn antisites on Cu as a typical example of a possible defect were estimated using the reference DLM state, the same as used above for the calculation of total energies of the Heisenberg model.

We shall start discussion by comparing exchange integrals of ideal CuMnSb obtained using different reference states, namely, the DLM, AFM111, and AFM100 states. The symmetry of the lattice in the AFM100 and AFM111

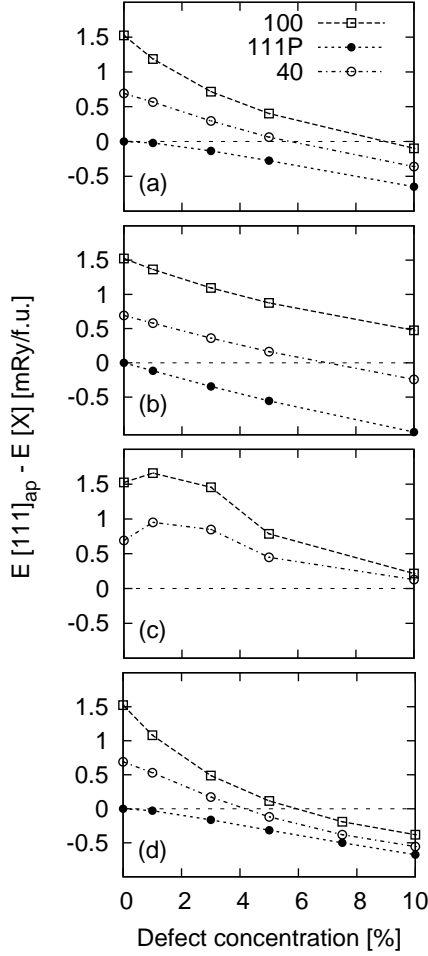


FIG. 4: The total energy differences $E[111]_{\text{ap}} - E[X]$ between the reference AFM111_{ap} state and other antiferromagnetic configurations for different defect concentrations of Mn antisites on Cu (a), Mn interstitials (b), Cu antisites on Mn (c) and for Cu↔Mn swap (d) as obtained from Heisenberg Hamiltonian calculations are shown. Index ap denotes the AFM phase with antiparallel alignment of defect Mn-moments to the moments on the native Mn-sublattice.

reference states is lower as compared to that in the DLM state. We therefore present their shell-averaged values. The shell-averaged $J_{ij}^{\text{Mn,Mn}}$ are obtained by summing up all interactions in a given shell with distance d divided by their number.

The result is shown in Fig. 5. We emphasize that the character of exchange interactions is very similar in spite of very different reference states. In particular, we note the negative (AFM-like) first and third NN interactions and the positive (FM-like) second NN interaction. The model Heisenberg Hamiltonian phase diagram for Heusler alloys assuming two or three NN was studied in Ref.23. A necessary condition for the formation of the AFM111-phase (and also for the AFM40 one) in the framework of the two NN model is the negative

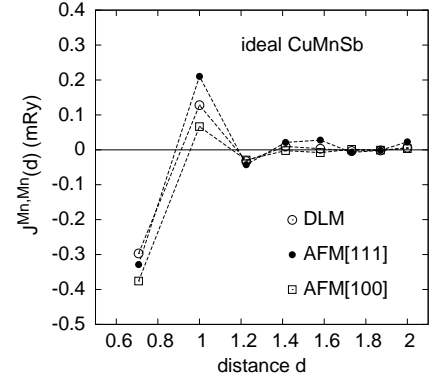


FIG. 5: Exchange integrals of the ideal CuMnSb as a function of the distance d (in units of the lattice constant) between Mn-moments evaluated using three different reference states, namely, the DLM-state, the AFM111, and AFM100 ones. In the latter two cases we present shell-averaged values (see text for details).

$J_2^{\text{Mn,Mn}}$. On the contrary, the negative $J_1^{\text{Mn,Mn}}$ and the positive $J_2^{\text{Mn,Mn}}$ stabilize the AFM100 phase. Calculated exchange integrals show, in agreement with the total energy calculations that the AFM100 phase has a lower total energy than AFM111 in the ideal CuMnSb alloy. This conclusion is confirmed for the model with up to 62 NN integrals used in the analysis of the ground state of the Heisenberg model.

There are three kinds of $J_{ij}^{\text{Mn,Mn}}$ for CuMnSb with the nonzero Mn_{Cu} -antisite concentrations x , namely, (i) between Mn-moments on the native Mn-sublattice (weight 1, no defects on the native lattice), (ii) between Mn-moments on the Cu-sublattice (weight x^2), and (iii) intersublattice ones, in which one moment is on the Mn-sublattice and the other on the Cu-sublattice (weight $2x$). Results are shown in Fig. 6 for interactions on the native Mn-sublattice and for intersublattice ones. The presence of defects strongly modifies the first two leading interactions. It should be noted that $J_2^{\text{Mn,Mn}}$ is reduced in its size and becomes comparable to $J_3^{\text{Mn,Mn}}$ and $J_4^{\text{Mn,Mn}}$. This indicates that also more distant interactions are important.

In particular, the strong weakening of FM-like $J_2^{\text{Mn,Mn}}$ interactions indicates destabilization of the AFM100 phase with increasing Mn antisite concentration x . The intersublattice interactions are shown in Fig. 6b. The leading intersublattice interaction is much stronger than on the native lattice (due to the reduction of NN Mn-Mn distance) and becomes strongly AFM-like with increasing concentration x . This is also true for the $J_2^{\text{Mn,Mn}}$ interaction although less pronounced. The interactions, whose weight increases with increasing concentration x , are responsible for the crossover to AFM111 phase. However, weakening of the positive $J_2^{\text{Mn,Mn}}$ with increasing concentration x also supports the crossover.

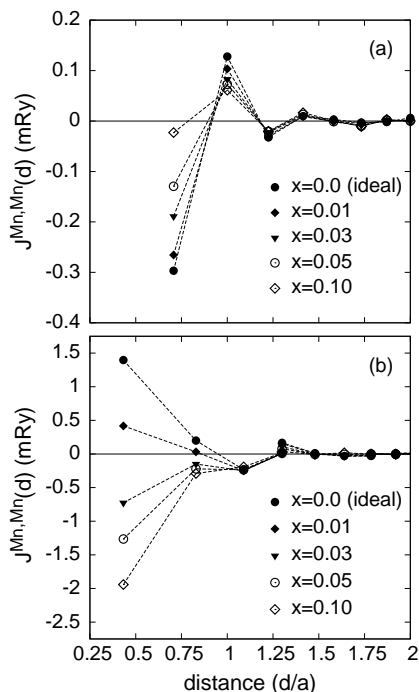


FIG. 6: Exchange interactions for CuMnSb with varying concentrations x of Mn antisites on Cu lattice as a function of the distance d between Mn-moments (in the units of the lattice constant) calculated by using the TB-LMTO-CPA-DLM-LDA+U method: Interactions among moments on the native Mn-sublattice (a), and Intersublattice interactions between Mn moments on Mn- and Cu-sublattices (b). The case $x=0$ corresponds in the framework of the CPA to the limit of two isolated Mn-moments.

E. Experiment

CuMnSb samples were prepared by direct synthesis from elements of the following purity: Cu (99.999%), Mn (99.98%) and Sb (99.999%), mixed in stoichiometric ratio 1:1:1. Samples were placed in Al_2O_3 crucibles in double sealed quartz ampoules under argon atmosphere and heated up to 1000°C at a rate of $1^\circ\text{C}/\text{min}$ and annealed for one day. Differential thermal analysis was carried out on Setaram SETSYS-2400 CS instrument. The crystal structure of the resulting sample was investigated by means of X-ray powder diffraction, using Bruker D8 Advance (Cu K_α radiation) diffractometer using full-profile Rietveld method. The X-ray pattern of a CuMnSb sample was indexed in a cubic unit cell (space group $F\bar{4}3m$ with the lattice parameter $a = 6.0974(3)$ Å). The absence of any additional reflections indicates that sample is single phase. Also the heat capacity measurements were performed in the temperature range 20 - 350 K by means of a Quantum Design PPMS equipment. For more details see Ref.5.

Time-of-flight neutron powder diffraction data were collected at the High Intensity Powder diffractometer (HIPD) at Los Alamos Neutron Science Center. Sets

of collected diffraction patterns from 6 detector banks ($\pm 40^\circ$, $\pm 90^\circ$, $\pm 153^\circ$) at different temperatures (10, 20, 30, 40, 50, 60, 70 and 100 K) were used for refinement. Data analysis was performed using FullProf software.²⁶ Possible magnetic arrangement was determined by irreducible representation analysis using SARA h software.²⁷

Structural refinement shows that structure is cubic with space group $F\bar{4}3m$ (216) and cell parameter for 100 K is $6.086(1)$ Å as was already reported.^{4,28} During the refinement a small discrepancy of intensities of main nuclear reflections was found. This can be due to the fact that the atomic occupancies can be different from the ideal - fully separated - one. Due to the fact that coherent scattering length of Mn ($b_c = -3.75$ fm), Sb ($b_c = 5.51$ fm) and Cu ($b_c = 7.72$ fm) are very different, the neutron diffraction data can provide very accurate information about the mixed site occupancy. Several possibilities were tested. The best fit of the experimental data was obtained by mixed occupancies Mn/Cu (Wyckoff position 4a) and Cu/Mn (Wyckoff position 4c). Constraints to site full occupancy and same occupancy ratio for both sites were applied. By refinement the mix/occupancy ratio was found to be $1.6(1)\%$ in a good agreement with results of presented theoretical calculations.

An apparition of magnetic reflections was observed on diffraction patterns bellow 50 K. These reflections can be indexed using magnetic propagation vector $q = (\frac{1}{2}\frac{1}{2}\frac{1}{2})$. This means that magnetic unit cell doubles the structural one in all three directions. From the irreducible representation (IR) analysis only two possible arrangements of spins for the Mn site (Wyckoff position 4a) are possible - Γ_2 and Γ_3 . Both solutions were tested, but only Γ_2 model was able to fit the experimental data. IR Γ_2 , AF111, is represented by (111) ferromagnetic planes with spins perpendicular to the plane which are stacked antiferromagnetically along [111] direction. The same configuration can be described by the magnetic space group $R\bar{7}3c$ (No. 161.72, setting $\frac{1}{2}a - \frac{1}{2}b$, $\frac{1}{2}b - \frac{1}{2}c$, $2a + 2b + 2c$). Calculated magnetic moment of Mn atoms at 10 K is $3.4(1) \mu_B$. This value is very close to $3.9(1) \mu_B$ obtained with neutron diffraction at 4 K and reported in Ref.4. The small discrepancy can be due to the different temperatures at which the neutron diffraction data were collected.

IV. CONCLUSIONS

The controversy between the experimentally observed AFM111 magnetic structure of CuMnSb and the total energy calculations which predict a different ground state for this material is resolved. Large residual resistivities observed experimentally indicate presence of structural defects due to the sample preparation. We suggest as an explanation the presence of defects in real material. We have therefore investigated from first principles the ground state of selected magnetic phases of CuMnSb alloy with defects using the supercell VASP total energy calculation and the model Heisenberg Hamiltonian

derived from the paramagnetic DLM state with no prescribed magnetic configuration. The Heisenberg Hamiltonian, determined from the paramagnetic state, was used to find possible candidates for the magnetic ground state. In all cases we used the LDA+U approach to treat approximately the effect of electron correlations in narrow Mn *d*-bands. The main conclusions are: (i) The magnetic ground state of ideal CuMnSb crystal is not the AFM111 phase; (ii) The experimentally observed AFM111 phase is the ground state of CuMnSb samples with Mn defects which occupy the nearest neighbor sites of the native Mn sublattice, namely, Mn-antisites on Cu lattice, and Mn-interstitials; (iii) The crossover to the AFM111 phase is due to the very strong AFM-like intersublattice interactions among the NN Mn-moments with distances shorter than those on the native Mn lattice. The weakening of the ferromagnetic 2nd NN interactions on the native Mn-lattice due to defects also helps to stabilize the AFM111 phase; (iv) The supercell approach gives critical concentrations for the crossover to AFM111 state below 3% for defects mentioned above while the Heisenberg model approach predicts the values at least two times larger; and (v) Neutron

diffraction experiment confirms the existence of low defect concentrations of about 2%. We conclude that the experimentally observed AFM111 phase is stabilized by defects, in particular those that form the NN pairs with Mn atoms on the native Mn sublattice (Mn antisites on Cu, Mn interstitials, and possibly also Cu \leftrightarrow Mn swaps).

Acknowledgments

We acknowledge the financial support from the Czech Science Foundation (Grant No. 14-37427G) and the National Grid Infrastructure MetaCentrum (project LM2010005) for access to computation facilities. This work has benefited from the use of HIPD at the Lujan Center at Los Alamos Neutron Science Center, funded by the DOE Office of Basic Energy Sciences. Los Alamos National Laboratory is operated by Los Alamos National Security LLC under DOE Contract No. DE-AC52-06NA25396.

-
- ¹ T. Graf, C. Felser, S. S. P. Parkin, *Progress in Solid State Chemistry* **39**, 1 (2011).
 - ² T. Jungwirth, X. Marti, P. Wadley, and J. Wunderlich, *Nature Nanotech.* **11**, 231 (2016).
 - ³ X. Marti, I. Fina, C. Frontera, J. Liu, P. Wadley, Q. He, R. J. Paull, J. D. Clarkson, J. Kudrnovský, I. Turek, J. Kuneš, D. Yi, J.-H. Chu, C. T. Nelson, L. You, E. Arenholz, S. Salahuddin, J. Fontcuberta, T. Jungwirth, and R. Ramesh, *Nat. Mater.* **13**, 367 (2014).
 - ⁴ R. H. Forster and G. B. Johnston, and D. A. Wheeler, *J. Phys. Chem. Solids* **29**, 855 (1968).
 - ⁵ F. Máca, J. Mašek, O. Stelmakhovych, X. Martí, H. Reichlová, K. Uhlířová, P. Beran, P. Wadley, V. Novák, and T. Jungwirth, *J. Magn. Magn. Mater.* **324**, 1606 (2012).
 - ⁶ P. Wadley, V. Novák, R. Campion, C. Rinaldi, X. Martí, H. Reichlová, J. Železný, J. Gazquez, M. Roldan, M. Varela, D. Khalyavin, S. Langridge, D. Kriegner, F. Máca, J. Mašek, R. Bertacco, V. Holý, A. Rushforth, K. Edmonds, B. Gallagher, C. Foxon, J. Wunderlich, and T. Jungwirth, *Nat. Commun.* **4**, 2322 (2013).
 - ⁷ T. Jeong, R. Weht, and W. E. Pickett, *Phys. Rev. B* **71**, 184103 (2005).
 - ⁸ J. Kudrnovský, V. Drchal, I. Turek, and P. Weinberger, *Phys. Rev. B* **78**, 054441 (2008).
 - ⁹ B. Alling, S. Shallcross, and I. A. Abrikosov, *Phys. Rev. B* **73**, 064418 (2006).
 - ¹⁰ J. Boeuf, C. Pfleiderer, and A. Faisst, *Phys. Rev. B* **74**, 024428 (2006).
 - ¹¹ G. Kresse and J. Furthmüller, *Phys. Rev. B* **54**, 11169 (1996).
 - ¹² I. Turek, V. Drchal, J. Kudrnovský, M. Šob, and P. Weinberger, *Electronic Structure of Disordered Alloys, Surfaces and Interfaces* (Kluwer, Boston, 1997).
 - ¹³ Z. W. Lu, S.-H. Wei, Alex Zunger, S. Frota-Pessoa, and L. G. Ferreira, *Phys. Rev. B* **44**, 512, (1991).
 - ¹⁴ A. I. Liechtenstein, M. I. Katsnelson, V. P. Antropov, and V. A. Gubanov, *J. Magn. Magn. Mater.* **67**, 65 (1987).
 - ¹⁵ I. Turek, J. Kudrnovský, V. Drchal, and P. Bruno, *Philos. Mag.* **86**, 1713 (2006).
 - ¹⁶ B. L. Gyorffy, A. J. Pindor, J. Staunton, G. M. Stocks, and H. Winter, *J. Phys. F: Metal Phys.* **15**, 1337 (1985).
 - ¹⁷ G. Kresse and D. Joubert, *Phys. Rev. B* **59**, 1758 (1999).
 - ¹⁸ P. A. Korzhavyi, A. V. Ruban, I. A. Abrikosov, and H. L. Skriver, *Phys. Rev. B* **51**, 5773 (1995).
 - ¹⁹ S. H. Vosko, L. Wilk, and M. Nusair, *Can. J. Phys.* **58**, 1200 (1980).
 - ²⁰ A. B. Shick, A. I. Liechtenstein, and W. E. Pickett, *Phys. Rev. B* **60**, 10 763 (1999).
 - ²¹ E. Sasioglu, I. Galanakis, C. Friedrich, and S. Blügel, *Phys. Rev. B* **88**, 134402 (2013).
 - ²² M. Yu. Lavrentiev, D. Nguyen-Manh, and S. L. Dudarev, *Phys. Rev. B* **81**, 184202 (2010).
 - ²³ J. L. Morán-López, R. Rodríguez-Alba, and F. Aguilera-Granja, *J. Magn. Magn. Mater.* **131**, 417 (1994).
 - ²⁴ J. P. Perdew and A. Zunger, *Phys. Rev. B* **23**, 5048 (1981); D. M. Ceperley and B. J. Alder, *Phys. Rev. Lett.* **45**, 566 (1980).
 - ²⁵ J. P. Perdew, K. Burke, and M. Ernzerhof, *Phys. Rev. Lett.* **78**, 1396 (1997).
 - ²⁶ J. Rodriguez-Carvajal, *Physica B* **192**, 55 (1993).
 - ²⁷ A. S. Wills, *Physica B* **276**, 680 (2000).
 - ²⁸ K. Endo, *J. Phys. Soc. Japan* **29**, 643 (1970).